# Optimal Inductor Design for 3-Phase Voltage-Source PWM Converters Considering Different Magnetic Materials and a Wide Switching Frequency Range

R. Burkart,
H. Uemura,
J. W. Kolar

# Optimal Inductor Design for 3-Phase Voltage-Source PWM Converters Considering Different Magnetic Materials and a Wide Switching Frequency Range

Ralph M. Burkart, Hirofumi Uemura and Johann W. Kolar

Power Electronic Systems Laboratory

ETH Zurich, Physikstrasse 3

Zurich, 8092, Switzerland

burkart@lem.ee.ethz.ch

*Abstract*—In this paper, an optimization regarding volume, efficiency and costs of AC boost inductors in 3-phase PWM converters based on detailed multi-domain models is presented. The optimization is performed for a wide switching frequency range of 5-80 kHz and a wide current ripple range of 5-100 %, considering ferrite, amorphous and powder core materials in combination with round, litz, foil and flat wire windings. The shown analysis and optimization identifies the best core material/winding type combinations for both thermally and efficiency-constrained inductor designs. Furthermore, the investigations reveal that simplified scaling assumptions, e.g. a proportional relationship between the inductor volume and the inverse of the frequency or the stored energy, are only accurate in special cases.

## I. INTRODUCTION

Magnetic components represent an integral part of almost any modern power electronic converter and are essential for their proper operation. Commonly known examples are transformers for galvanic isolation and voltage adaption, AC and DC chokes in switched-mode power converters or differential-(DM) and common-mode (CM) inductors for EMI filtering. Typically, the magnetic components do not only use a considerable share of the total converter volume but also cause high relative costs with respect to other components [1]–[5]. Consequently, performance optimizations (e.g. regarding volume, cost, efficiency) of magnetic components is a commonly seen topic in literature. Beyond the optimization of application-specific magnetic components with comparably few and narrow design parameter ranges, there is also an interest for general scaling laws and knowledge about the trade-offs of magnetics as illustrated by the following examples.

In [6]–[8], inductor scaling laws are considered to minimize the volume of DC chokes in DC/DC converters or the inductive components of EMI filters. All contributions assume a simplified linear relationship between volume and stored magnetic energy. In [9] and [10], multi-level multi-cell PFC AC/DC converters are discussed. There, the number of employed converter cells in series and/or parallel has a significant impact on the AC choke(s) requirements. As a consequence, a detailed understanding of the inductor performance trade-offs within wide frequency and current-ripple ranges is essential for the proper optimization of such systems. Finally, with the introduction of SiC power transistors the frequency-volume-dependency of inductors has recently also gained importance, e.g. for photovoltaic power converters. In this area, it has

not yet quantitatively been clarified whether the volume and cost savings on inductors due to higher switching frequencies enabled by SiC can compensate the increased semiconductor costs [2], [11]–[15].

The above discussion and examples motivate for a systematic investigation of the trade-offs, scaling laws and limitations of magnetic components based on detailed multi-domain physical models rather than simplified assumptions. An early attempt to achieve this can be found in [16], where an optimization tool for litz wire ferrite core transformers is employed for performance investigations for frequencies from 100 kHz to 1 MHz. [17] presents a systematic optimization algorithm for inductors in different application areas with foil and round wire. Advanced loss and reluctance models are described but results are not shown. In [18], the volume scaling of DC/DC converter chokes is presented. Both frequency (5-80 kHz) and current ripple ratio (10-50 %) variations and different core materials are considered while no information is given on the modeling. Finally, [19]–[21] present DC choke optimizations for wide frequency (20-150 kHz) and current ripple ratio (10-220 %) ranges, forced and natural convection cooling and a wide variety of core materials. However, only foil windings are considered and the results are given as only indicative core-window area-products from which the underlying geometries and the final volumes cannot be uniquely inferred.

In this paper, a systematic and comprehensive performance analysis is presented. It includes the consideration of

- a wide frequency range of 5-80 kHz,
- a wide current ripple ratio range of 5-100 %,
- ferrite, amorphous iron and powder core materials and
- round, litz, foil and flat wires.

In contrast to the aforementioned studies, AC boost inductors in 20 kW 3-phase 3-level voltage-source PWM converters are analyzed. The objective is the investigation of scaling laws regarding

- the volume of thermally constrained designs,
- the volume of efficiency-constrained designs and
- total inductor costs,

employing advanced and experimentally verified multi-domain models and loss data from measurements. Natural convection cooling and a fixed inductor geometry are considered.

In **Sec. II**, the general system specifications are described. **Sec. III** presents a detailed discussion of the employed models.
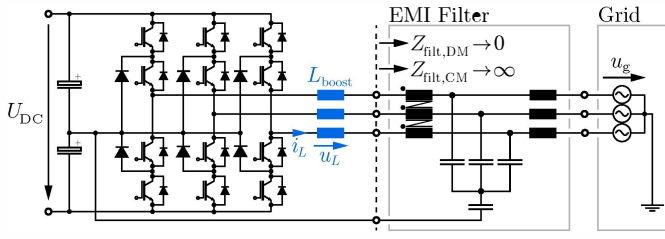
**Fig. 1:** Typical 3-phase 3-level voltage-source PWM inverter in a grid-side application. For the investigation of the performance trade-offs of the boost inductors $L_{boost}$ regarding volume, efficiency and costs, the specifications listed in **Tab. I** are considered. The EMI filter is assumed to be ideal, i.e. zero DM and infinite CM impedance $Z_{filt,DM} \to 0$ and $Z_{filt,CM} \to \infty$, respectively, is seen from the converter side.

**Tab. I:** Specifications of the converter system depicted in **Fig. 1**.

| | | | |
|---|---|---|---|
| General | Rated power | $P_r$ | 20 kW |
| | Fundamental phase current | $\hat{I}_{L(1)}$ | 41 A |
| | DC-link voltage | $U_{DC}$ | 650 V |
| | Grid line-voltage | $\hat{U}_g$ | $(230 \cdot \sqrt{2})$ V |
| | Grid frequency | $f_g = f_1$ | 50 Hz |
| Control | Modulation signal [22] | | Sinusoidal with 3$^{rd}$ harmonic injection |
| | Modulation depth | $M$ | 1.0 |
| | Switching frequency | $f_{sw}$ | 5–80 kHz |

Finally, in **Sec. IV**, the results of the comparative evaluation and the investigated scaling laws are presented.

## II. SYSTEM SPECIFICATIONS

**Fig. 1** shows the analyzed boost inductors in a typical grid-side application (e.g. solar inverters, input stage of uninterruptible power suplies). A 3-phase 3-level voltage-source PWM converter employing a sinusoidal PWM control scheme with third harmonic injection was selected [22]. The EMI filter, which is normally required to meet the applicable EMC directives, is assumed to feature ideal characteristics, i.e. the DM impedance seen from the converter side approaches zero while the CM impedance is very high and suppresses any CM currents. Accordingly, the inductor voltage $u_L$ equals the whole DM voltage generated by the converter, while the generated CM voltage fully applies to the EMI filter. Note that this assumption is usually met with good accuracy for optimized filters [23].

## III. INDUCTOR MODELING

In this section, the employed multi-domain models are discussed in detail. **Sec. III-A** presents the used reluctance model. **Sec. III-B** and **Sec. III-C** describe the core and winding loss and cost models. Finally, in **Sec. III-D** the considered thermal model is presented.

It is expected, that the fundamental trade-offs (e.g. losses versus volume) and physics of inductors are largely invariant from the selected core geometry (e.g. E-cores, U-cores). Therefore, for simplicity reasons, the symmetric EE-core inductor geometry as depicted in **Fig. 2** is assumed throughout this work. The available effective window area is equal for all analyzed winding types.
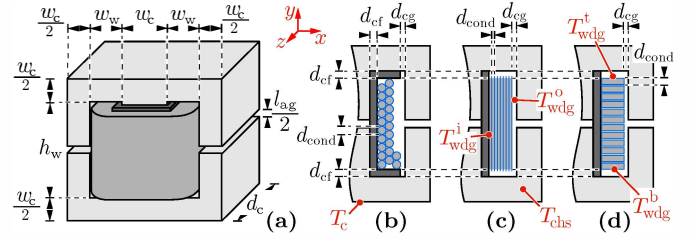


**Fig. 2:** Assumed inductor geometry. **(a)** Symmetric EE-core geometry with equal air gap lengths for all legs, center leg width $w_c$, core depth $d_c$, total air gap length $l_{ag}$, window width $w_w$ and window height $h_w$. **(b)** Round and litz wire winding geometry with conductor diameter (copper and insulation) $d_{cond}$, coil former with constant thickness $d_{cf}$ and gap between core and winding $d_{cg}$. **(c)** Foil and **(d)** flat wire winding geometry with equal gaps to the core as for round/litz wire. The figure furthermore depicts the location of the modeled temperatures of the thermal network model (**Fig. 5**).

### A. Reluctance Model

The reluctance model of the shown inductor in **Fig. 2** can be described by the equation

$$N_{wdg} \cdot i_L = \Phi \cdot \left( R_{mag,c} \left( \frac{\Phi}{k_{fill,c} A_c} \right) + R_{mag,ag} \right), \qquad (1)$$

where $N_{wdg}$ is the number of winding turns. The above model is non-linear due to the non-linear dependency of the core reluctance $R_{mag,c}$ from the the flux density $B = \frac{\Phi}{k_{fill,c} A_c}$,

$$R_{mag,c}(B) = \frac{l_{mag,c}}{\mu_0 \, \mu_r(B) \, k_{fill,c} A_c} . \qquad (2)$$

The product $k_{fill,c} A_c$ is the effective core cross section taking into account the core filling factor. The relative core permeability $\mu_r$ can equivalently be expressed as a function of the magnetic field $H$ or the flux density $B$. An accurate calculation of the magnetic path length $l_{mag,c}$ including the treatment of the core corner sections can be found in [24]. The reluctance $R_{mag,ag}$ of the air gaps is calculated based on a 3D application of the Schwartz-Christoffel-transformation, which takes into account the 3D geometry and gives accurate results also for large relative air gap lengths. Formulas and experimental verifications can be found in [25].

### B. Core Models

*1) Core Materials:* **Tab. II** lists the considered core materials along with the physical parameters as used in this work. The selected materials are commonly used in industry and literature and are thus representative candidates for each of the considered fundamental material types: ferrites, tape-wound amorphous iron cores and powder cores. High-performance nanocrystalline materials, such as the Vitroperm500F from Vacuumschmelze, have not been analyzed due their high relative costs [5] and the generally poor availability of cut cores (such as E-cores) as a result of the material's brittleness. Iron powder cores and laminated steel have been neglected for this first analysis due to the comparably high core losses. A detailed discussion of the selected material's properties along with a wide range of other materials can be found in [26].

*2) Core Loss Models:* For the given application, the material is excited by a LF 50 Hz (ideally) sinusoidal voltage and superimposed HF square-wave voltage pulses resulting from the switched-mode operation of the converter. Therefore, on

the one hand, the core loss model comprises a LF component where the generalized Steinmetz equation (GSE) is used,

$$P_{\text{c,LF}} = k_{\text{fill,c}} V_{\text{c}} \cdot k\, f_{\text{g}}^{\alpha}\, \hat{B}^{\beta}\ , \tag{3}$$

where $k$, $\alpha$ and $\beta$ are the Steinmetz parameters. On the other hand, the a HF component is included in the core loss model which employs the improved improved generalized Steinmetz equation (i$^2$GSE) for square-wave excitations [24],

$$P_{\text{c,HF}} = k_{\text{fill,c}} V_{\text{c}} \cdot f_{\text{g}} \sum_i \overline{k}_i \left| \frac{1}{\Delta T_i} \right|^{\alpha_i} |\Delta B_i|^{\beta_i}\ , \tag{4}$$

with

$$\overline{k} = \frac{k_i}{(2\pi)^{\alpha_i - 1} \int_0^{2\pi} |\cos\theta|_i^{\alpha}\, 2^{\beta_i - \alpha_i} \mathrm{d}\theta}\ . \tag{5}$$

The parameters $k_i$, $\alpha_i$ and $\beta_i$ are operating-point-dependent Steinmetz parameters which take into account the influence of the premagnetization $H_{\text{DC}}$ and the tempereture $T_{\text{c}}$. $\Delta B_i$ denotes the peak-to-peak flux density swings of the piecewise linear HF flux segments and $T_i$ the corresponding time intervals ($\sum T_i = 1/f_{\text{g}}$).

*3) Calculation of Core Losses:* The approach taken for the core loss calculation is illustrated in **Fig. 3**.

The sinusoidal LF loss contribution is normally small. Therefore, for reasons of simplicity, the Steinmetz parameters for sinusoidal excitations provided in the respective data sheets are used. In contrast, the HF losses are mostly dominant and are caused by square-wave voltage pulses. Therefore, more care is required to obtain accurate results. For this work, the hybrid loss map approach presented in [24] is employed. The approach includes experimentally determined losses for different operating points characterized by the quadruple $(\Delta B, f, T_{\text{c}}, H_{\text{DC}})$. For any operating point of interest $(\Delta B_i, f_i, T_{\text{c},i}, H_{\text{DC},i})$, the closest measurements in the loss map are used to extract (local) Steinmetz parameters $(\overline{k}_i, \alpha_i, \beta_i)$ which can then be used for a loss interpolation by means of the i$^2$GSE (4). A detailed analysis of the performed loss measurements and the achievable accuracy is presented in [24].

The LF flux amplitude $\hat{B}$ can be calculated by means of the reluctance model (1), while the linear HF flux density swings $\Delta B_i$ can be calculated by

$$\Delta B_i = \frac{\Delta\Psi_i}{N_{\text{wdg}}\, k_{\text{fill,c}}\, w_{\text{c}}\, d_{\text{c}}} = \frac{1}{N_{\text{wdg}}\, k_{\text{fill,c}}\, A_{\text{c}}} \cdot \int_{t_{i-1}}^{t_i} u_L(t)\,\mathrm{d}t\ . \tag{6}$$

The volt-second pulses $\int_{t_{i-1}}^{t_i} u_L(t)\,\mathrm{d}t$ can either be obtained by means of a circuit simulator or an equivalent model-based algorithm as described in [27].

*4) Cost Model:* A linear cost model for the core material costs is assumed as proposed in [5],

$$\Sigma_{\text{c}} = \sigma_{\text{mat,c}}\, W_{\text{c}}\ , \tag{7}$$

where $\sigma_{\text{mat,c}}$ are relative costs per core weight $W_{\text{c}}$ (cf. **Tab. II**).

*5) Model Limitations:* The employed core models exhibit the following limitations:

- **Loss maps:** loss maps are so far only available for the materials N87 and 2605SA1. Therefore, for the KoolMµ materials, the premagnetization- and
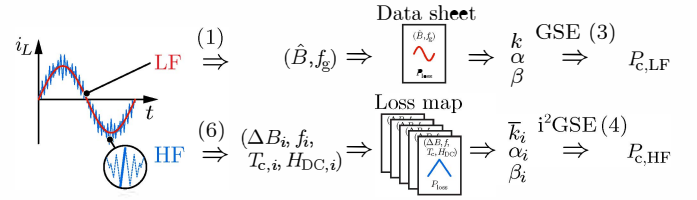


**Fig. 3:** Core loss computation approach. Using the reluctance model (1), the fundamental LF flux density amplitude $\hat{B}$ can be calculated from the current waveform $i_L(t)$. The LF core losses $P_{\text{c,LF}}$ are then calculated based on the data sheet Steinmetz parameters for sinusoidal excitations and the GSE (3). For each linear HF flux density segment $(\Delta B_i, f_i, T_{\text{c},i}, H_{\text{DC},i})$, operating-point-dependent Steinmetz parameters $(\overline{k}_i, \alpha_i, \beta_i)$ are extracted from a loss map consisting of core loss measurements for different operating points. Finally, the HF core losses $P_{\text{c,HF}}$ can be estimated with the i$^2$GSE (4) for square-wave excitations.

**Tab. II:** Properties of the considered core materials, taken from [5], [28]–[30]. $B_{\text{sat}}$ denotes the saturation flux density. $\mu_{\text{r}}(H = 0)$ is the initial permeability, $T_{\text{chs,max}}$ the maximum permissible hot spot operating temperature, $\lambda_{\text{th,c}}$ the thermal conductivity, $k_{\text{fill,c}}$ the effective core fill factor (mainly relevant for laminated materials), $\rho_{\text{c}}$ the material volumetric density and $\sigma_{\text{mat,c}}$ the relative costs. Soft saturation is given if the material's $B$-$H$ curve has a soft roll-off, which makes the materials suitable for non-linear inductance designs.

| Core material: | N87 | 2605SA1 | KoolMµ 40µ/ 60µ |
|---|---|---|---|
| Type | Ferrite bulk | Amorphous laminated | Powder bulk |
| Manufacturer | EPCOS | Metglas | Magnetics |
| Composition | MnZn | Fe-B-Si | Fe-Al-Si |
| Air gap | Yes | Yes | No |
| Loss map | Yes | Yes | No |
| Soft saturation | No | Yes | Yes |
| $B_{\text{sat}}$ @ $T_{\text{chs,max}}$    (T) | 0.39 | 1.42 | 1.00 |
| $\mu_{\text{r}}(H = 0)$ @ $T_{\text{chs,max}}$ | 1590 | 55650 | 39/58 |
| $T_{\text{chs,max}}$    (°C) | 100 | 150 | 200 |
| $\lambda_{\text{th,c}}$ (W/m K) | 4.18 | 9/5 [1)] | 8 |
| $k_{\text{fill,c}}$ | 1.00 | 0.83 | 1.00 |
| $\rho_{\text{c}}$    (kg/m$^3$) | 4850 | 7180 | 6000/6800 |
| $\sigma_{\text{mat,c}}$ (€/kg) | 5.5 | 16 | 20 |

[1)] Along/perpendicular to lamination

temperature-independent Steinmetz parameters for sinusoidal excitation from the data sheet were used for both LF and HF loss calculations. This is supported by measurements on comparable powder core materials which suggest, that the premagnetization-dependency of the KoolMµ materials is negligible [24].

- **Gap losses:** several contributions have reported increased losses of tape-wound materials (such as 2605SA1) in the presence of air gaps and fringing fields [26], [31], [32]. However, detailed systematic data or models, in particular for the 2505SA1 material, could not be found in literature and was neither available through own measurements. Therefore, in order to prevent significant underestimations of the respective losses, the zero-air-gap loss-map-based calculated 2505SA1 core losses were multiplied by a factor $k_{\text{2605SA1}} = 1.5$ throughout this work.

- **Non-linearity:** for simplicity reasons, the HF excitations (inductor volt-second pulses $\int_{t_{i-1}}^{t_i} u_L(t)\,\mathrm{d}t$) are calculated assuming a linear, current-independent inductance $L_0$. In

the case of non-linear inductances $L \equiv L(i_L)$, the 3-phase system shown in **Fig. 1** becomes asymmetric. As a result, involved analysis and/or simulations would be required to determine the correct waveform of $u_L$.

### C. Winding Models

*1) Winding types:* The considered winding types and properties are listed in **Tab. III**. For the winding geometries refer to **Fig. 2**.

*2) Winding Loss Models:* Using the Maxwell equations, it can be shown that the general solution for the losses of an arbitrarily shaped single conductor $x$ (solid or litz wire) in the presence of a sinusoidal current with frequency $f$ are always of the form

$$P_{\mathrm{wdg}}^{x}(T_{\mathrm{wdg}}, f) = R_{\mathrm{DC}}(T_{\mathrm{wdg}}) \cdot X^{*}\big(\xi_{x}(T_{\mathrm{wdg}}, f)\big) \cdot \hat{I}_{L(f)}^{2}, \quad (8)$$

where $R_{\mathrm{DC}}$ is the conductor DC resistance. $\xi_{\mathrm{x}}$ is a function of the conductor copper diameter $d_{\mathrm{cond,cop}}$ and the skin depth $\delta_{\mathrm{cop}}$,

$$\xi_{\mathrm{x}} = \frac{d_{\mathrm{cond,cop}}}{\sqrt{2}\,\delta_{\mathrm{cop}}} = d_{\mathrm{cond,cop}} \cdot \sqrt{\frac{\pi f \mu_0 \, \sigma_{\mathrm{cop}}(T_{\mathrm{wdg}})}{2}} \, . \quad (9)$$

For the different winding types, different approaches were chosen to determine the unknown geometry-dependent function $X^{*}$.

- **Round and litz:** for round and litz wire conductors, well-known and tractable analytical solutions exist based on 1D field approximations. The solutions for $X^{*}$ distinguish between skin and proximity effect losses and are of the form,

$$X^{\{\mathrm{ro,li}\}}\big(\xi_{\{\mathrm{ro,li}\}}\big) = $$
$$\big[F_{\mathrm{skin}}^{\{\mathrm{ro,li}\}}(\xi_{\{\mathrm{ro,li}\}}) + G_{\mathrm{prox}}^{\{\mathrm{ro,li}\}}(\xi_{\{\mathrm{ro,li}\}})\big] \cdot \overline{H}_{\mathrm{ext}(f)}^{2} \, . \quad (10)$$

  The exact expressions for $F_{\mathrm{skin}}^{\{\mathrm{ro,li}\}}$ and $G_{\mathrm{prox}}^{\{\mathrm{ro,li}\}}$ can e.g. be found in [17] or [24]. The approach to calculate the required normalized external field $\overline{H}_{\mathrm{ext}(f)}$ is presented below.

- **Foil and flat:** Investigations, e.g. found in [17] or [24], show that an accurate analytical determination of $X^{*}$ is highly complex for foil and flat wire geometries. This is mainly due to the fact that 2D fields must be described as 1D approximation result in large errors. As a consequence, a pragmatic and more accurate approach based on finite-element (FEM) simulations was pursued to model $X^{*}$ by means of interpolated FEM results. Note that the FEM simulations must only sweep over a few *relative* geometric parameters and a sufficiently wide range of frequencies, as the relationship between $f$, $T_{\mathrm{wdg}}$ and $d_{\mathrm{cond,cop}}$ is known (9). This reduces the computational effort by $\mathcal{O}(n^2)$.

*3) Calculation of Winding Losses:* The winding losses must be calculated for each winding turn and frequency separately, using the above derived loss formula (8). Furthermore, it must be distinguished between the part of the winding inside the core window and the part outside the window.

The 50 Hz fundamental current amplitude $\hat{I}_{L(1)}$ is given in **Tab. I**, while the HF switching frequency harmonics $\hat{I}_{L(f)}$ of
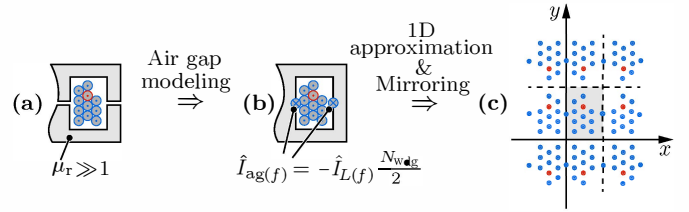


**Fig. 4:** Method of images (mirroring) used for the calculation of the normalized external fields $\overline{H}_{\mathrm{ext}(f)}$ in round and litz wire windings. **(a)** Round wire winding inside the winding window. **(b)** The fringing field of the air gaps can be modeled with equivalent currents generating a similar field distribution. **(c)** The impact of the core material ($\mu_{\mathrm{r}} \gg 1$, e.g. $\mu_{\mathrm{r}} > 20$) is imitated by mirrored conductors. The individual conductors are modeled as point-currents (1D approximation) and the external field $\overline{H}_{\mathrm{ext}(f)}$ in the center of a conductor of interest can be calculated with (11). In this work, 3 mirroring steps are performed as an analysis has shown that the accuracy cannot significantly be improved with a higher number of steps.

**Tab. III:** Properties of the considered winding types. The geometric data is taken from standards and data sheets. Note that $d_{\mathrm{cond}}$ includes both copper thickness and insulation increase, i.e. $d_{\mathrm{cond}} = d_{\mathrm{cond,cop}} + d_{\mathrm{cond,ins}}$. Litz wires from [33] with strand diameters $d_{\mathrm{cond,s}}$ of {40,50,71,100,200,355} μm (AWG {46,44,41,38,32,27}) were considered . The number of strands $N_{\mathrm{strand}}$ for a given diameter $d_{\mathrm{cond}}$ was calculated based on fitted data sheet information [33]. The thermal conductivities are taken from data sheets, simulations and measurements. Finally, the cost data is from [5]. IACS copper with an electrical conductivity of $\sigma_{\mathrm{cop}}(T = 20\,^{\circ}\mathrm{C}) = 5.8 \cdot 10^{8}$ S and a density of $\rho_{\mathrm{cop}} = 8890\,\mathrm{kg/m^3}$ was assumed.

| Winding type: | Round | Litz | Foil | Flat |
|---|---|---|---|---|
| $d_{\mathrm{cond,min}}$ (mm) | 0.50 | 0.50 | 0.05 | 1.25 |
| $d_{\mathrm{cond,max}}$ (mm) | 5.00 | 5.00 | 1.25 | $(1{:}2)^{1)}$ |
| Insulation type | Enamel [34] | Silk [33] | Kapton [35] | Enamel/air |
| Ins. increase (mm) | 0.025-0.049 | 0.0375 | 0.025 | 0.25 |
| $T_{\mathrm{wdghs,max}}$ (°C) | $150^{2)}$ | $150^{2)}$ | $150^{2)}$ | $150^{2)}$ |
| $\lambda_{\mathrm{th,wdg}}$ (W/m K) | $1.0^{3)}$ | $0.3^{3)}$ | $401/0.37^{4)}$ | $401/0.03^{4)}$ |
| $\sigma_{\mathrm{mat,wdg}}$ (€/kg) | 10.0 | $\frac{15.0}{\frac{A_{\mathrm{strand}}}{\mathrm{mm}^2}+0.45}$ | 20.0 | 10.0 |
| $\Sigma_{\mathrm{mat,wdg}}^{\mathrm{fc}}$ (€/unit) | 1.0 | 1.0 | 2.0 | 2.0 |
| $\sigma_{\mathrm{lab,wdg}}$ (€/kg) | 7.0 | 7.0 | 14.0 | 21.0 |
| $\Sigma_{\mathrm{lab,wdg}}^{\mathrm{fc}}$ (€/unit) | 2.0 | 2.0 | 2.5 | 4.0 |

$^{1)}$ Ratio between $d_{\mathrm{cond}}$ and conductor width
$^{2)}$ Limited due to the considered coil formers [28] ($\lambda_{\mathrm{th,cf}} = 0.3\,\mathrm{W/mK}$)
$^{3)}$ For a hexagonal winding arrangement including air (cf. **Fig. 2**)
$^{4)}$ IACS copper / insulation material

the given system can be computed using the analytical methods presented in [22] or by means of simulations.

The required normalized field amplitude $\overline{H}_{\mathrm{ext}(f)}$ in (10) at the position $\vec{r}$ of a conductor of interest can be approximated by means of a superposition of all occurring fields at this position,

$$\overline{H}_{\mathrm{ext}(f)}(\vec{r}) = \frac{1}{\hat{I}_{L(f)}} \cdot \left| \sum_{i}^{N^{*}} \check{H}_{i(f)}(\vec{r}) \right| . \quad (11)$$

The $N^{*}$ field sources partly result from the $(N_{\mathrm{wdg}}-1)$ currents in the neighboring winding turns as shown in **Fig. 4(a)**. The remaining sources result from the employed method of images (mirroring) as described in [24], which can accurately take into account the impact of air gap fringing fields **Fig. 4(b)** and the core material **Fig. 4(c)** on $\overline{H}_{\mathrm{ext}(f)}$.

An accuracy analysis based on 2D FEM simulations showed very good agreement with the litz and round wire loss models

described above. The observed error was always below 5 % for high-permeability materials (N87 and 2605SA1) and below 10 % for the low-permeability materials (KoolMμ 40μ and 60μ). A similar analysis and results can be found in [24]. The results of the accuracy analysis imply that despite the underlying assumption of the mirroring method of ideal high-permeability core materials with $\mu_r \to \infty$, $\mu_r > 20$ is sufficient in practice to achieve high accuracy.

The statistical mean error introduced by the interpolation approach for foil and flat wire conductors is below 3 % with maximum errors of 20 % in special cases. Note that no extrapolation was necessary for all results shown in this work.

*4) Cost Model:* The winding costs can be estimated using the model presented in [5],

$$\Sigma_{wdg} = (\sigma_{mat,wdg} + \sigma_{lab,wdg}) \cdot W_{wdg} + \Sigma^{fc}_{mat,wdg} + \Sigma^{fc}_{lab,wdg} \ . \quad (12)$$

The parameters $\sigma_{mat,wdg}$ and $\sigma_{lab,wdg}$ are specific material and labor costs per weight $W_{wdg}$ and $\Sigma^{fc}_{mat,wdg}$ and $\Sigma^{fc}_{lab,wdg}$ are fixed material and labor costs (e.g. coil former, connectors).

*5) Model Limitations:* The main limitation of the presented winding models is the calculation of the HF current harmonics $\hat{I}_{L(f)}$ for which the analytical method presented in [22] is employed. The method is accurate for linear inductors (error < 5 %) but cannot take into account non-linear inductor behavior.

### D. Thermal Model

The employed thermal model in this work is based on the empirical models presented in [36]. Modifications were introduced in order to account for anisotropic, direction-dependent thermal properties of the used materials.

*1) Thermal Resistance Network:* The thermal resistance network of the modified thermal model is shown in **Fig. 5**. The underlying inductor geometry is depicted in **Fig. 2**. The winding hot spot temperature is, based on measurements, assumed to be on the outer surface of the winding, while the core hot spot location is assumed to be in the center of the core. Different winding surface temperatures (inner, outer, top, bottom) are modeled, whereas, for simplicity reasons, a uniform core surface temperature is assumed.

*2) Heat Transfer Mechanisms:* 3 different types of heat transfer mechanisms are considered for the resistances shown in **Fig. 5**. For the thermal constants and parameters used in the below equations, please refer to **Tab. V**.

- **Conduction:** the thermal resistance which models conducted heat transfer is given by

$$R_{th,cond} = \frac{l_*}{\lambda_{th,*} \cdot A_*} \ , \quad (13)$$

where $\lambda_{th,*}$ is the material's thermal conductivity (cf. **Tab. II** and **Tab. III**) and $l_*$ and $A_*$ the (direction-dependent) length and cross section of the heat conductor to be modeled.

- **Radiation:** radiated heat from an object 1 to an object 2 can be modeled with the thermal resistance,

$$R_{th,rad} = \frac{1}{h_{rad,*} \cdot A_*} = \frac{T_{1,*} - T_{2,*}}{\epsilon_{1,*} \cdot \sigma \left(T^4_{1,*} - T^4_{2,*}\right)} \cdot \frac{1}{A_*} \ . \quad (14)$$

where $h_{rad,*}$ represents the heat transfer coefficient, $A_*$ is the overlapping area of the two objects and $T_{1,*} > T_{2,*}$ are the respective temperatures.
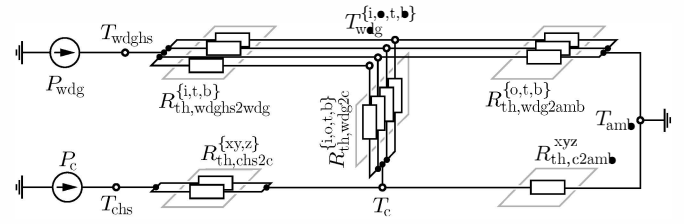


**Fig. 5:** Anisotropic modified thermal model based on the empirical models in [36]. $P_{wdg}$ and $P_c$ are the total winding and total core losses, respectively. $R^{\{i,t,b\}}_{th,wdghs2wdg}$ are the thermal resistances from the winding hot spot, which is assumed to be on the outer winding surface, to the respective inner, top and bottom winding surface. $R^{\{i,o,t,b\}}_{th,wdg2c}$ and $R^{\{o,t,b\}}_{th,wdg2amb}$ are the resistances from the winding surfaces to the core surface and to the ambient, respectively. The inner winding surface is not exposed to the ambient. $R^{\{xy,z\}}_{th,chs2c}$ and $R^{xyz}_{th,c2amb}$ are the resistances from the core hot spot to the core surface with uniform temperature $T_c$ and from the surface to the ambient. The corresponding geometry of this network is depicted in **Fig. 2**.

**Tab. IV:** Modeled heat transfer mechanisms in the thermal network depicted in **Fig. 5**. Conducted heat transfer between the winding and the core is only applicable where the winding touches the core. This depends on the specific winding geometry and type (cf. **Fig. 2**).

| Resistances: | $R^{\{i,t,b\}}_{th,wdghs2wdg}$ | $R^{\{xy,z\}}_{th,chs2c}$ | $R^{\{i,o,t,b\}}_{th,wdg2c}$ | $R^{\{o,t,b\}}_{th,wdg2amb}$ | $R^{xyz}_{th,c2amb}$ |
|---|---|---|---|---|---|
| **Conduction** | ✓ | ✓ | Partly | | |
| **Radiation** | | | ✓ | ✓ | ✓ |
| **Convection** | | | | ✓ | ✓ |

**Tab. V:** Thermal parameters and constants employed in the empirical thermal model of this work (taken from [36]).

| | | |
|---|---|---|
| Emissivity of enameled copper | $\epsilon_{wdg}$ | 0.8 |
| Emissivity of the core materials | $\epsilon_{wdg}$ | 0.9 |
| Stephan-Boltzmann constant | $\sigma$ | $5.67 \cdot 10^{-8}$ W/m$^2$ K$^4$ |
| Vertical-positioning coefficient | $C_v$ | 1.58 |
| Reference pressure (sea level) | $p_{ref}$ | 101.32 kPa |
| Reference ambient temperature | $T_{amb,ref}$ | $(25 + 273.15)$ K |

- **Natural convection:** natural convection is considered where the transfer coefficient $h_{rad,*}$ in (14) changes to

$$h_{conv,*} = C_v \left(\frac{p}{p_{ref}}\right)^{0.477} \left(\frac{T_{amb}}{T_{amb,ref}}\right)^{-0.218} \frac{(T_* - T_{amb})^{0.225}}{L^{0.285}_{ch}} \ . \quad (15)$$

In the above equation (15), $L_{ch}$ is the characteristic length which for the given inductor geometry was approximated with

$$L_{ch} \approx d_c + (h_w - 2d_{cf}) + 2\sqrt{w^2_w + (\frac{w_c}{2} + d_{cf})^2} \ . \quad (16)$$

Most of the thermal resistances depicted in the thermal network model in **Fig. 5** combine more than one of the above mechanisms. The total resistances shown in **Fig. 5** can be calculated by the parallel connection of the individual type-specific resistances,

$$\frac{1}{R_{th,tot}} = \frac{1}{R_{th,cond}} + \frac{1}{R_{th,rad}} + \frac{1}{R_{th,conv}} \ . \quad (17)$$

The applicable types of heat transfer of each of the thermal resistances depend on the specific geometry and/or winding type and are listed in **Tab. IV**.
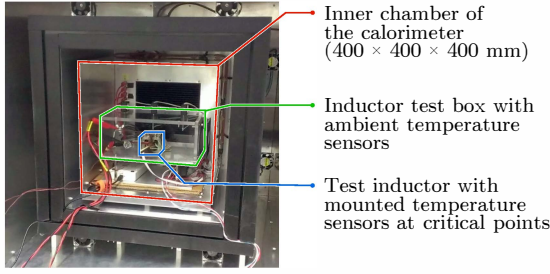
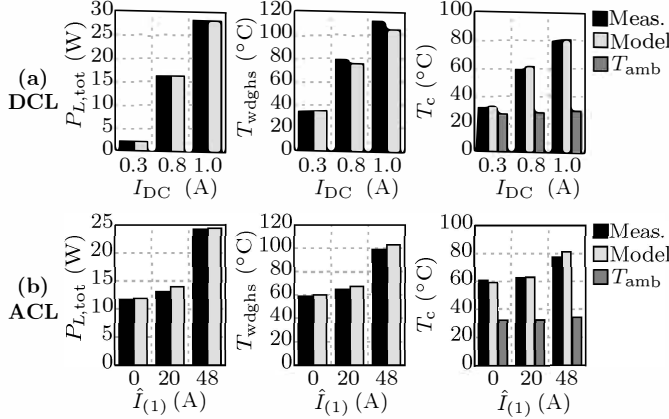Fig. 6: Experimental inductor loss and temperature measurement setup.



Fig. 7: Results of the experimental verification of the proposed thermal and loss models based on the inductor designs of **Tab. VI**. **(a)** Verification of the thermal model only, using different DC currents $I_{DC}$ in conjunction with a known DC winding resistance $R_{DC}(T_{wdg})$. **(b)** Combined verification of the thermal and loss models, using different 50 Hz LF AC currents $\hat{I}_{(1)}$ superimposed by a 9.5 A/16 kHz peak-to-peak HF current. Deviations of less than 10 % between actual and calculated temperatures/losses were observed.

**Tab. VI:** Test inductor design parameters for the experimental verification of the thermal and loss models shown in **Fig. 7**. The high DC resistance of the DCL inductor winding results from the large number of winding turns ($N_{wdg} > 300$) which was used to experimentally determine the thermal conductivity $\lambda_{th,wdg}$ of hexagonal round wires (cf. **Tab. III**).

| Inductor name: | DCL | ACL |
|---|---|---|
| Core material | N87 | 2605SA1 |
| Core size | E80/38/20 (1 set × 3 stacked) | AMCC06R3 (2 sets × 2 stacked) |
| Air gap length $l_{ag}$ | None | 1.0 mm |
| Winding type | Round | Round |
| $R_{DC}(T_{wdg} = 25\,°C)$ | 21.2 Ω | 7.8 mΩ |
| LF current | 0 Hz (DC) | 50 Hz |
| HF current | None | 16 kHz / 9.5 A |

*3) Experimental verification:* In order to verify the accuracy of the thermal model, the temperature and loss measurement setup depicted in **Fig. 6** has been implemented. Measurements have been performed on several inductors, such as the two test inductors with parameters as listed in **Tab. VI**. In a first experiment (DCL), only DC currents without superimposed HF currents were used **Fig. 7(a)**. This allows to evaluate the performance of the thermal model only due to the negligibly uncertainty regarding the driving losses. In a second experiment (ACL), LF AC currents with a superimposed HF current component were used to verify the performance

**Tab. VII:** Considered optimization constraints in addition to the core, winding and system constraints/specifications (**Tab. I-III**). The geometric constraints reflect typical properties of available EE-cores [28]–[30] with a stacking factor of 3 cores.

| | | | |
|---|---|---|---|
| **General** | Ambient Temperature | $T_{amb}$ | 40 °C |
| | Ambient air pressure | $T_{amb}$ | 97.7 kPa |
| | Max. inductance decrease | $L_{min}/L_{\bullet} = L(I_{L,max})/L(0)$ | 50 % |
| | Max. flux density | $B_{max}/B_{sat}$ | 90 % |
| **Geometry** | Window ratio | $h_w/w_w$ | 3 |
| | Core width ratio | $w_c/w_w$ | $\sqrt{2}$ |
| | Core depth | $d_c/w_c$ | 3 |
| | Coil former ratio | $d_{cf}/w_w$ | 1/5 |
| | Core gap ratio | $d_{gc}/w_w$ | 1/20 |
| | Max. air gap ratio | $l_{ag}/w_c$ | 1/2 |

of the combined loss and thermal models **Fig. 7(b)**. In all analyzed operating points deviations of less than 10 % between measurement and calculation were observed.

## IV. Comparative Evaluation

In this section, the results of a comparative evaluation of the selected materials and winding types regarding achievable performance (volume, efficiency, costs) is presented. Furthermore, general scaling laws are investigated. For simplicity reasons, a fixed inductor geometry as described in **Tab. VII** is assumed where only the boxed inductor volume $V_L$ is continuously varied. It is expected that the volume most significantly affects the inductor performance, while other geometric parameters have only a subordinate influence. The parameters in **Tab. VII** were chosen based on typical available E-cores. The chosen stacking factor/core depth $d_c$ yields a close to maximum area product for a given volume $V_L$.

### A. Performance Analysis

In **Fig. 8**, the minimum achievable volumes are compared where the required efficiency is unconstrained. As a result, most designs operate at the thermal limit. An exception are the KoolMµ designs for low-frequency/low-ripple conditions due to the missing degree of freedom of the air gap and the maximum permissible inductance drop constraint of 50 % (cf. **Tab. VII**). Amongst all possible options, the combinations of flat and foil windings with 2605SA1 cores achieve the lowest volumes. The main limitation of N87 is the low saturation flux density $B_{sat}$ and low maximum hot spot temperature $T_{chs,max}$ (cf. **Tab. II**) which cannot be compensated by the almost negligible core losses. Despite similar core losses, 2605SA1 outperforms the KoolMµ materials due to a higher $B_{sat}$, better temperature exploitation and the fact. Moreover, like the KoolMµ materials, 2605SA1 also features a soft roll-off of the $B$-$H$ curve (cf. **Tab. II**, [29]). This feature can be utilized to decrease the inductor volume by means of allowing the inductance to drop a certain percentage (here 50 %) at the inductor peak current [30], [37].

Similar performance results are obtained for efficiency-constrained designs as depicted in **Fig. 9**. However, 2605SA1 partly looses its dominance in high-ripple conditions where N87 and the KoolMµ materials feature a higher efficiency and hence lower volumes.

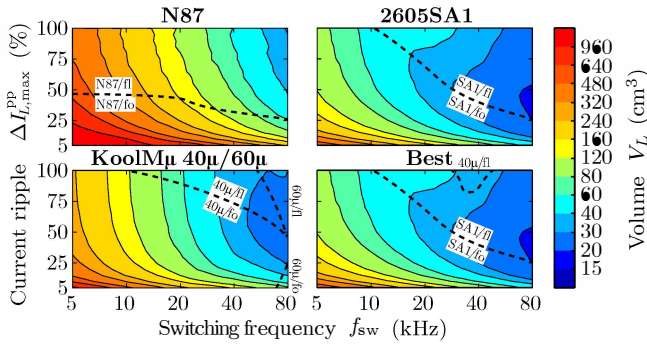In **Fig. 10**, a cost analysis of the thermally-constrained designs (**Fig. 8**) is shown. Despite slightly higher resulting

**Fig. 8:** Achievable minimum boxed volumes $V_L$ as a function of the maximum peak-to-peak current ripple ratio $\Delta I_{L,\max}^{\mathrm{pp}}$ and the converter switching frequency $f_{\mathrm{sw}}$ ($\log_2$-scaling for $f_{\mathrm{sw}}$ and $V_L$). All designs except the KoolMµ inductors are thermally constrained. For each material, only the best performing winding options are shown. These are without exception foil ("fo") and flat ("fl") wires mainly due to the superior filling factors and thermal advantages. Flat wire generally shows lower HF losses and is therefore better suited in high frequency/high ripple conditions. As recommended in the data sheet [30], the lower permeability powder core material KoolMµ 40µ is better suited for inductors with large energies $E_L = \int_0^{I_{L,\max}} L(i_L) i_L \, di_L$. The best overall option for all operating conditions is 2605SA1 with a foil/flat wire winding mainly due to the highest saturation flux density, a high maximum core temperature and comparably low core losses. The inductor losses here (best case) range from 7.5 W (smallest design) to 5l W (largest design).
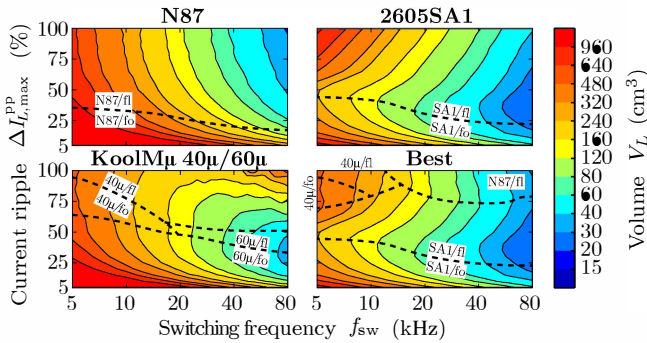


**Fig. 9:** Achievable minimum volumes $V_L$ for efficiency-constrained designs with a maximum permissible loss power of $P_L \leq 7\,\mathrm{W}$ ($\eta \geq 99.9\,\%$), considering all 3 inductors $L_{\mathrm{boost}}$). By inspection of **Fig. 8**, it can be seen that partially significantly larger volumes results than for thermally constrained designs, while flat and foil windings still offer the best performance for all materials. Regarding the overall optimum, powder (KoolMµ) and the low-loss ferrite (N87) cores partly supersede the 2605SA1-based designs for the high-ripple conditions. This can mainly be explained by the fact, that 2605SA1 cannot exploit the temperature advantage as for thermally constrained designs. For the best inductor designs, the winding hot spot temperatures $T_{\mathrm{w,ghs}}$ are between 53 °C and 139 °C.

**Fig. 10:** Achievable minimum total inductor costs $\Sigma_L$ for the *volume* optimized designs depicted in **Fig. 8**. It can be seen that round wires ("ro") generally outperform other winding types, which implies that the lower volume achieved by e.g. flat or foil (**Fig. 8**) windings is not sufficient to compensate for the higher losses. For high frequency/high ripple conditions, the volume difference between N87-based designs (larger) with respect to 2605SA1-based designs (smaller) becomes small enough to yield lower costs for N87.



**Fig. 11:** Scaling analysis of the inductor volume $V_L$ as a function of the converter switching frequency $f_{\mathrm{sw}}$ and the maximum stored inductor energy $E_L = \int_0^{I_{L,\max}} L(i_L) i_L \, di_L$ for efficiency- and thermally constrained designs. None of the depicted combinations of foil winding with N87 and 2605SA1 have a constrained air gap length or winding geometry. The volumes scale approximately with $f^{-1}$ in a limited range, where the HF losses (in particular the core losses) are small when compared to the total losses. The same applies to the volume-energy scaling. The low-loss N87 shows a largely proportional dependency between stored energy and volume in a wide range of the realized inductance $L$ and current ripples $\Delta I_L$. On the other hand, the lossier 2605SA1 clearly deviates from this proportionality in high ripple/high frequency conditions.

volumes than for flat/foil wire solutions, round wires in combination with 2605SA1 or N87 are generally the least expensive option.

*B. Scaling Laws*

**Fig. 11** shows the scaling of the volume as a function of the frequency and the maximum stored inductor energy. The examples of foil windings in combination with N87 and 2605SA1 demonstrate, that the often used simplified scalings laws – volume proportional to the inverse of the frequency $V_L \propto f^{-1}$ or proportional to the stored energy $V_L \propto E_L$ – are only good approximations in special cases where the HF core and winding losses are small when compared to the total losses. This is mostly the case for N87 and 2605SA1 in
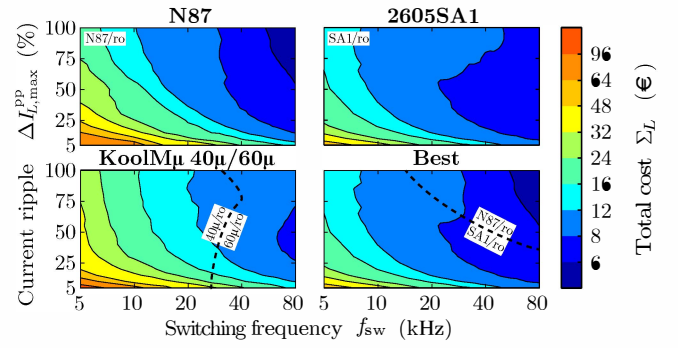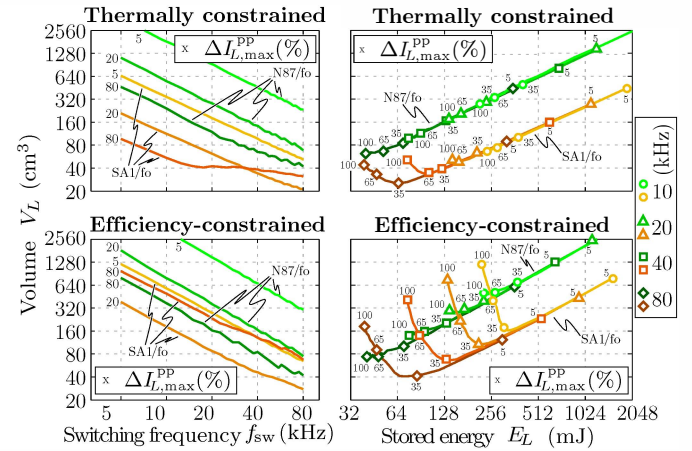
low frequency/low ripple conditions. For N87 it is expected, that the simplified scaling laws also loose accuracy for higher frequencies or AC only applications. The scaling of the KoolMµ materials is generally highly non-linear (**Fig. 8** and **Fig. 9**).

## V. CONCLUSION

In this paper, a systematic multi-objective analysis and comparison regarding volume, efficiency and costs of AC boost chokes in 3-phase 3-level switched-mode PWM converters is presented. Ferrite, amorphous and powder cores in combination with round, litz, foil and flat wire windings were considered. Detailed multi-domain models, which are verified by means of experimental measurements and FEM

simulations, were used.

The comparative analysis showed a generally superior performance of the amorphous material 2605SA1 for this kind of application. The combination with flat wire and foil windings allows for the lowest achievable volumes in a wide frequency and current ripple range, while a combination with round wire results in the lowest costs. An investigation of the volume scaling as a function of the frequency and the stored inductor energy revealed, that the often used assumptions of a volume proportional to the inverse of the frequency or to the stored energy are only accurate in special cases, i.e. under the condition of low relative HF losses.

Future research continuing this work can be divided into 4 categories.

- **Applications:** the derived models can be used to investigate the trade-offs and Pareto-fronts of both standard and novel applications, e.g. multi-level multi-cell converters or high-switching-frequency SiC PV inverters.
- **Investigations:** more detailed investigations can be performed with the optimization tool as described in this work, e.g. the analysis of the influence of different core geometries (other core shapes, varying core proportions) or the consideration of other core materials.
- **Model extensions:** in order to overcome the limitations of the employed models, loss maps with experimentally determined losses for the powder core materials should be established. Furthermore, the influence of air gaps and fringing fields on tape-wound core losses must be investigated in detail. The present linear approach for the calculation of the HF currents and flux density swings should be replaced by an approach which enhances the accuracy for non-linear, current-dependent inductors. Moreover, the thermal model can be modified to include forced convection cooling and heat sinking of the core and winding.
- **Model verifications:** Finally, implementations of inductors made of different materials and winding types should be used for a combined verification of the derived models, which have so far mostly been separately verified.

### REFERENCES

[1] G. Gong, M. L. Heldwein, U. Drofenik, J. Miniböck, K. Mino, and J. W. Kolar, "Comparative Evaluation of Three-Phase High-Power-Factor AC-DC Converter Concepts for Application in Future More Electric Aircraft," *IEEE Trans. IE*, vol. 52, no. 3, pp. 727–737, June 2005.
[2] B. Burger, D. Kranzer, and O. Stalter, "Cost Reduction of PV-Inverters with SiC-DMOSFETs," in *Proc. CIPS*, pp. 1–6, June 2008.
[3] J. Biela, U. Badstübner, and J. W. Kolar, "Impact of Power Density Maximization on Efficiency of DC-DC Converter Systems," *IEEE Trans. PE*, vol. 24, no. 1, pp. 288–300, Jan. 2009.
[4] Y. Wang, S. W. H. De Haan, and J. Ferreira, "Potential of Improving PWM Converter Power Density with Advanced Components," in *Proc. EPE*, pp. 1–10, Sept. 2009.
[5] R. M. Burkart and J. W. Kolar, "Component Cost Models for Multi-Objective Optimizations of Switched-Mode Power Converters," in *Proc. ECCE*, Sept. 2013.
[6] J. Kassakian, M. F. Schlecht, and G. C. Verghese, *Principles of Power Electronics*. Prentice Hall, 1991.
[7] D. L. Loree and J. P. O'Loughlin, "Design Optimization of L-C Filters," in *Proc. PMS*, pp. 137 –140, June 2000.
[8] K. Jalili and S. Bernet, "Design of $LCL$ Filters of Active-Front-End Two-Level Voltage-Source Converters," *IEEE Trans. IE*, vol. 56, no. 5, pp. 1674–1689, May 2009.
[9] H. Ertl, J. W. Kolar, and F. C. Zach, "Analysis of a Multilevel Multicell Switch-Mode Power Amplifier Employing the "Flying-Battery" Concept," *IEEE Trans. IE*, vol. 49, no. 4, pp. 816–823, Aug. 2002.
[10] M. Kasper, D. Bortis, and J. Kolar, "Scaling and Control of Multi-Cell Converters," in *Proc. IPEC*, May 2014.
[11] D. Kranzer, C. Wilhelm, F. Reiners, and B. Burger, "Application of Normally-off SiC-JFETs in Photovoltaic Inverters," in *Proc. EPE*, pp. 1–6, Sept. 2009.
[12] C. Wilhelm, D. Kranzer, and B. Burger, "Development of a Highly Compact and Efficient Solar Inverter with Silicon Carbide Transistors," in *Proc. CIPS*, March 2010.
[13] S. Araújo, C. Nöding, B. Sahan, and P. Zacharias, "Exploiting the Benefits of SiC by Using 1700 V Switches in Single-Stage Inverter Topologies Applied to Photovoltaic Systems," in *Proc. PCIM Europe*, May 2011.
[14] R. Mallwitz, C. Althof, S. Buchhold, and E. Kiel, "First 99% PV Inverter with SiC JFETs on the Market – Future Role of SiC," in *Proc. PCIM Europe*, May 2012.
[15] R. M. Burkart and J. W. Kolar, "Comparative Evaluation of SiC and Si PV Inverter Systems Based on Power Density and Efficiency as Indicators of Initial Cost and Operating Revenue," in *Proc. COMPEL*, June 2013.
[16] S. A. Mulder, "On the Design of Low-Profile High Frequency Transformers," in *Proc. HFPC*, pp. 141–159, 1990.
[17] P. Wallmeier, N. Fröhleke, and H. Grotstollen, "Automated Optimization of High Frequency Inductors," in *Proc. IECON*, vol. 1, pp. 342–347 vol.1, Aug. 1998.
[18] H. Sartori, H. Hey, and J. Pinheiro, "An Optimum Design of PFC Boost Converters," in *Proc. EPE*, pp. 1–10, Sept. 2009.
[19] B. Lyons, J. Hayes, and M. Egan, "Magnetic Material Comparisons for High-Current Inductors in Low-Medium Frequency DC-DC Converters," in *Proc. APEC*, pp. 71–77, Feb. 2007.
[20] M. Ryłko, B. Lyons, K. Hartnett, J. Hayes, and M. Egan, "Magnetic Material Comparisons for High-Current Gapped and Gapless Foil Wound Inductors in High Frequency DC-DC Converters," in *Proc. EPE-PEMC*, pp. 1249–1256, Sept. 2008.
[21] M. Ryłko, K. Hartnett, J. Hayes, and M. Egan, "Magnetic Material Selection for High Power High Frequency Inductors in DC-DC Converters," in *Proc. APEC*, pp. 2043–2049, Feb. 2009.
[22] R. M. Burkart and J. W. Kolar, "Low-Complexity Analytical Approximations of Switching Frequency Harmonics of 3-Phase $N$-Level Voltage-Source PWM Converters," in *Proc. IPEC*, May 2014.
[23] D. O. Boillat, J. W. Kolar, and J. Mühlethaler, "Volume Minimization of the Main DM/CM EMI Filter Stage of a Bidirectional Three-Phase Three-Level PWM Rectifier System," in *Proc. ECCE*, pp. 2008–2019, Sept. 2013.
[24] J. Mühlethaler, "Modeling and Multi-Objective Optimization of Inductive Power Components," Ph.D. dissertation, ETH Zurich, 2012.
[25] J. Mühlethaler, J. W. Kolar, and A. Ecklebe, "A Novel Approach for 3D Air Gap Reluctance Calculations," in *Proc. ECCE Asia*, pp. 446–452, May 2011.
[26] M. Ryłko, B. Lyons, J. Hayes, and M. Egan, "Revised Magnetics Performance Factors and Experimental Comparison of High-Flux Materials for High-Current DCDC Inductors," *IEEE Trans. PE*, vol. 26, no. 8, pp. 2112–2126, Aug. 2011.
[27] M. Schweizer, T. Friedli, and J. W. Kolar, "Comparison and Implementation of a 3-Level NPC Voltage Link Back-to-Back Converter with SiC and Si Diodes," in *Proc. APEC*, pp. 1527–1533, Feb. 2010.
[28] EPCOS. SIFERRIT Material N87. [Online]. Available: http://www.epcos.com, Feb. 2014.
[29] Metglas. POWERLITE Inductor Cores. [Online]. Available: http://www.metglas.com, Feb. 2014.
[30] Magnetics. Powder Core Catalog 2013. [Online]. Available: http://www.magnetics.com, Feb. 2014.
[31] H. Fukunaga, T. Eguchi, Y. Ohta, and H. Kakehashi, "Core Loss in Amorphous Cut Cores with Air Gaps," *IEEE Trans. Magn.*, vol. 25, no. 3, pp. 2694–2698, 1989.
[32] B. Cougo, A. Tüysüz, J. Mühlethaler, and J. W. Kolar, "Increase of Tape Wound Core Losses Due to Interlamination Short Circuits and Orthogonal Flux Components," in *Proc. IECON*, vol. 1, pp. 123–128 vol.1, 2011.
[33] Pack Feindrähte. RUPALIT Classic Litz Wires. [Online]. Available: http://www.pack-feindraehte.de, Dec. 2013.
[34] *Specifications for Particular Types of Winding Wires – Part 0-1: General Requirements – Enamelled Round Copper Wire*, IEC 60317-0-1, 2008.
[35] Bridgeport Magnetics Group. LAMINAX Winding Conductors. [Online]. Available: http://www.alphacoredirect.com, Feb. 2014.
[36] A. van den Bossche and V. C. Valchev, *Inductors and Transformers for Power Electronics*. Taylor & Francis, 2005.
[37] A. Stadler and C. Gulden, "Efficient Nonlinear Inductors for PV Inverters and Active PFC," in *Proc. CIPS*, March 2012.